The Planetary Science Journal, 3:59 (20pp), 2022 March https://doi.org/10.3847/PSJ/ac53ad

New Constraints on Titan's Stratospheric *n*-Butane Abundance

Brendan L. Steffens[1,2], Conor A. Nixon[2], Keeyoon Sung[3], Patrick G. J. Irwin[4], Nicholas A. Lombardo[5], and Eric Pereira[1]

[1] Florida Institute of Technology, 150 West University Boulevard, Melbourne, FL 32901, USA
[2] NASA Goddard Space Flight Center, Planetary Systems Laboratory, Code 693, Greenbelt, MD 20771, USA
[3] Jet Propulsion Laboratory, California Institute of Technology, 4800 Oak Grove Drive, Pasadena, CA 91109, USA
[4] Department of Physics, University of Oxford, Oxford OX1 2JD, UK
[5] Department of Earth and Planetary Sciences, Yale University, New Haven, CT 06511, USA
Received 2021 July 26; revised 2022 February 7; accepted 2022 February 8; published 2022 March 9

Abstract

Curiously, *n*-butane has yet to be detected at Titan, though it is predicted to be present in a wide range of abundances that span over 2.5 orders of magnitude. We have searched infrared spectroscopic observations of Titan for signals from *n*-butane (*n*-C_4H_{10}) in Titan's stratosphere. Three sets of Cassini Composite Infrared Spectrometer Focal Plane 4 (1050–1500 cm^{-1}) observations were selected for modeling, having been collected from different flybys and pointing latitudes. We modeled the observations with the Nonlinear Optimal Estimator for MultivariatE Spectral AnalySIS radiative transfer tool. Temperature profiles were retrieved for each of the data sets by modeling the ν_4 emission from methane near 1305 cm^{-1}. Then, incorporating the temperature profiles, we retrieved abundances of all of Titan's known trace gases that are active in this spectral region, reliably reproducing the observations. We then systematically tested a set of models with varying abundances of *n*-butane, investigating how the addition of this gas affected the fits. We did this for several different photochemically predicted abundance profiles from the literature, as well as for a constant-with-altitude profile. Ultimately, though we did not produce any firm detection of *n*-butane, we derived new upper limits on its abundance specific to the use of each profile and to multiple different ranges of stratospheric altitudes. These results will tightly constrain the C_4 chemistry of future photochemical modeling of Titan's atmosphere and also motivate the continued search for *n*-butane and its isomer, isobutane.

Unified Astronomy Thesaurus concepts: Titan (2186); Saturnian satellites (1427); Solar system (1528); Planetary science (1255); Planetary atmospheres (1244); Atmospheric composition (2120); Natural satellite atmospheres (2214)

1. Introduction

Titan, Saturn's largest moon, possesses a thick atmosphere composed primarily of molecular nitrogen (N_2) and methane (CH_4) at approximate stratospheric mixing ratios of 0.984 and 0.0148, respectively (Niemann et al. 2010). Additional hydrocarbons and nitriles, present in trace abundances at Titan, are the product of photochemistry initialized by solar UV radiation and charged particles gathered by Saturn's magnetic field. Simple hydrocarbons and nitriles form at the top of the atmosphere as the products of photodissociation of N_2 and CH_4; these proceed to recombine in a series of chain reactions as they diffuse downward, inevitably forming larger and more complex species, culminating in Titan's well-known stratospheric haze layers (Yung et al. 1984; Krasnopolsky 2009; Loison 2019; Vuitton et al. 2019). The result is an impressively diverse atmosphere with a wide variety of trace constituents, rich organic chemistry, the aforementioned haze and aerosol layers, and even clouds (Coustenis & Taylor 2008). This complex atmosphere is understood to serve as a potential analog of the early Earth's prebiotic atmosphere, making a present-day laboratory available in which to observe and study the conditions that may have contributed to biogenesis (Trainer 2013).

Our work has focused on the (possible) role of one particular gas in this complex atmosphere, namely, *n*-butane (*n*-C_4H_{10}: CH_3–CH_2–CH_2–CH_3). The abundances of many of Titan's other trace hydrocarbons and nitriles (as well as their spatial/temporal dependencies, in many cases) have already been investigated extensively through photochemical modeling work (Yung et al. 1984; Lara et al. 1996; Krasnopolsky 2009; Li et al. 2015; Dobrijevic et al. 2016; Willacy et al. 2016; Loison 2019; Vuitton et al. 2019), and many of these trace gases have already been detected. For example, benzene (C_6H_6) was detected by the Infrared Space Observatory (Coustenis et al. 2003), propene (C_3H_6) was detected by the Cassini Composite Infrared Spectrometer (CIRS; Nixon et al. 2013), propadiene (C_3H_4) was detected by NASA's Infrared Telescope Facility (IRTF; Lombardo et al. 2019b), acetonitrile (CH_3CN) was detected by the Institute for Radio Astronomy in the Millimeter Range (Bézard et al. 1993), and, using the Atacama Large Millimeter/submillimeter Array, ethyl cyanide (C_2H_5CN), vinyl cyanide (C_2H_3CN), and, most recently, cyclopropenylidene (*c*-C_3H_2) and methylcyanoacetylene (CH_3C_3N) have been detected as well (Cordiner et al. 2015; Palmer et al. 2017; Nixon et al. 2020; Thelen et al. 2020).

The butane molecule (Figure 1) has been predicted to be present in detectable abundances in Titan's atmosphere. In spite of this, it remains elusive to remote detection efforts, though its abundance has been constrained by Hewett et al. (2020), who found an upper limit of 513 ppb. Photochemically predicted abundances for butane at 200 km in altitude range from order 1

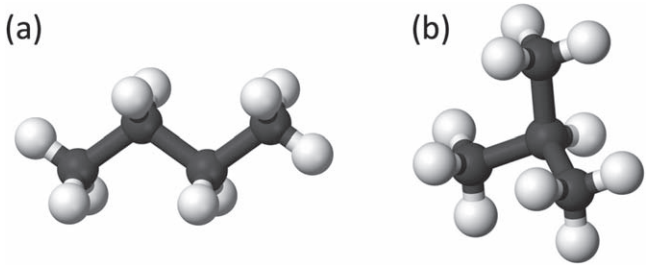

Figure 1. Molecular geometry of the target of our investigation: (a) *n*-C_4H_{10} (*n*-butane), contrasted with its spectroscopically distinct isomer, (b) isobutane, $HC(CH_3)_3$.

(Krasnopolsky 2009) to 370 ppb (Loison 2019) to even as high as 1100 ppb (Dobrijevic et al. 2016). The wide range of abundances seen here reflect the current state of uncertainty with respect to *n*-butane's role in Titan's atmosphere and chemistry. In fact, some photochemical models for Titan's atmosphere that include C_4 chemistry offer the disclaimer that their C_4 chemistry is largely incomplete (Yung et al. 1984); firm detection and measurement of *n*-butane is a reasonable and important first step toward mitigating this weakness in photochemical models. Additionally, evidence also suggests that butane molecules may play a role in the nucleation of Titan's hazes (Curtis et al. 2005). Thus, constraining the abundance of butane molecules may yield improved understanding of haze formation at Titan and elsewhere. Similarly, constraining the abundance of these larger molecules is likely to contribute to an improved understanding of atmosphere-to-surface transfer interactions (Lopes et al. 2010).

As a useful comparison to motivate interest in detecting butane, the similar hydrocarbon propane (C_3H_8) has been unambiguously detected in Titan's stratosphere in the infrared; moreover, it has been detected at similar abundances to those predicted for butane. Detection of propane was tentatively first accomplished in the early 1980s via Voyager 1's Infrared Interferometer Spectrometer instrument (Maguire 1981). A more robust detection of propane was then achieved in 2003 at an abundance of 620 ± 120 ppb using the ν_{26} band at 748 cm^{-1} (Roe 2003). Propane was then measured again in 2009 at an abundance of 420 ± 50 ppb using the ν_{26} band once again and simultaneously measured at an abundance of 570 ± 80 ppb using the ν_{18} band at 1376 cm^{-1} (Nixon et al. 2009). Considering the similar abundances predicted for propane and butane and the repeated success in measuring propane, butane's elusiveness to detection is indeed an anomaly worthy of investigation.

According to Vuitton et al. (2019), butane formation in Titan's atmosphere is likely to occur via the addition of methyl and propyl radicals. The propyl radicals are initially formed from propane via

$$C_2H + C_3H_8 \rightarrow C_3H_7 + C_2H_2 \quad (1)$$

or hydrogen addition to propene (C_3H_6), the latter of which has already been detected and measured by Nixon et al. (2013):

$$H + C_3H_6 \xrightarrow{M} C_3H_7. \quad (2)$$

Then, with the addition of the methyl radical, butane is formed:

$$C_3H_7 + CH_3 \xrightarrow{M} C_4H_{10}. \quad (3)$$

It is important to note that these reactions (and photochemical models in general) do not distinguish between the two isomers *n*-butane and isobutane. Thus, photochemically predicted abundances for C_4H_{10} are interpreted as being composed of the populations of both isomers. Though both isomers possess distinct infrared signals that are, in principle, detectable at Titan, we have focused our search on the *n*-butane isomer due to the availability of a recently developed high-resolution pseudoline list (Sung et al. 2020), but also because laboratory simulations of Titan's atmosphere have suggested a favored production of *n*-butane over isobutane (Ádámkovics 2003). Additionally, *n*-butane has been shown to dominate the higher-order hydrocarbons produced when ethane (C_2H_6) ices are irradiated at cold temperatures (Kim et al. 2010); isobutane was not detected as a product of that process.

It is expected that butane, if present in Titan's atmosphere, will follow the observed trend of enhanced hydrocarbon abundances at polar latitudes versus equatorial latitudes, particularly during the Titan winter. The observed enrichment in trace gases near Titan's winter pole is likely caused by a meridional overturning circulation in Titan's stratosphere that delivers low-latitude upper stratospheric air to the winter middle stratosphere, where it can be trapped by the stratospheric polar vortex (Sharkey 2021). Though some trace gases (notably CO_2) do seem to be an exception to this rule, we note that this trend has been observed for propyne (C_3H_4; Teanby et al. 2019), which, according to Vuitton et al. (2019), acts as a precursor to the propene reactant in Equation (2) via

$$C_3H_4 + H_2 \rightarrow C_3H_6. \quad (4)$$

We have modeled three distinct sets of infrared observations of Titan obtained by Cassini CIRS (Flasar et al. 2004; Jennings et al. 2017), one of them being equatorial and the other two from northern polar latitudes. This paper is organized as follows. In Section 2, we describe the Cassini CIRS observations, and in Section 3, we describe the process that we used to model these observations. In Section 4, we display the results of our work, followed by a discussion of these results and their implications for future work in Section 5. In Section 6, we present our conclusions and summarize the contents of this paper. Finally, the Appendix contains our full plotted results for each of the three sets of observations and the three different abundance profiles that we tested.

2. Observations

The limb observations of Titan were obtained by the CIRS instrument from Focal Plane 4 (FP4, 1050–1500 cm^{-1}; Flasar et al. 2004; Jennings et al. 2017) on board the Cassini spacecraft, which executed numerous flybys of Titan during its approximately 13 yr tour of the Kronian system. The CIRS was a remote-sensing Fourier transform spectrometer covering a wide infrared spectral range of 10–1500 cm^{-1}, with variable spectral resolutions between 0.5 and 15.5 cm^{-1}. Its observations have been used extensively in the past toward detecting and mapping Titan's trace atmospheric constituents (Nixon et al. 2009; Teanby et al. 2009; Cottini et al. 2012; Vinatier et al. 2015; Coustenis et al. 2016, 2018; Lombardo et al. 2019a; Teanby et al. 2019; Mathé et al. 2020; Vinatier et al. 2020).

We analyzed three sets of limb observations from different Cassini flybys. These flybys and the relevant details of the resulting data sets are contained in Table 1. We selected one

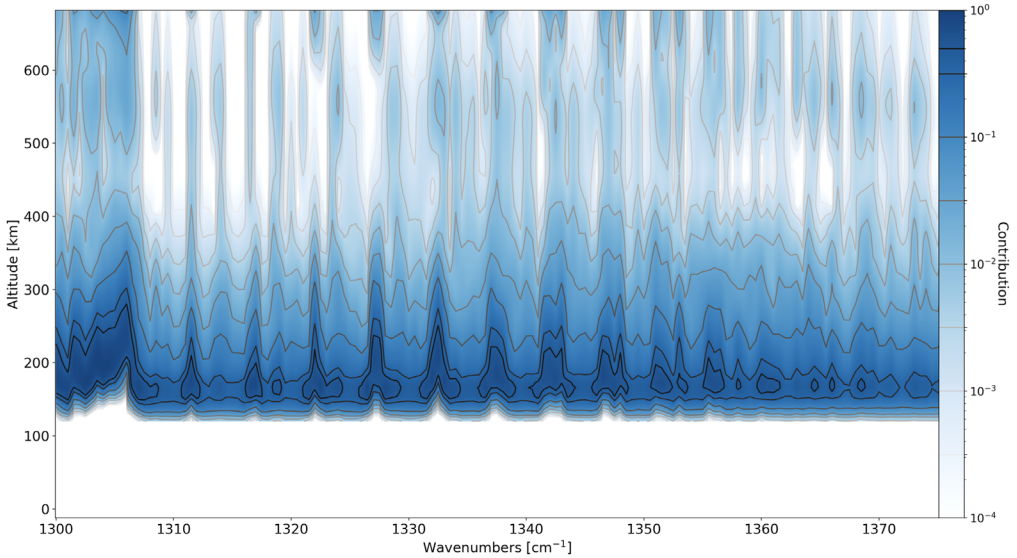

Figure 2. Normalized temperature contribution contours for the 136–216 km EQ data, showing particularly large sensitivity in that altitude range.

Table 1
Cassini CIRS Observations

Observations	Date	Season	L_S	Start Time	Hours	Latitude	Detector Footprint (km)
T3	2/15/05	N. winter	305°	19:57:53	4	82°N	50
T35	8/31/07	N. winter	345°	21:32:34	4	70°N	50
EQ	2004–2010	⋯	277°–9°	⋯	⋯	30°S–10°N	40

Note. The final column shows the average projected detector footprint for the observation set. We note that Titan's atmospheric scale height is approximately 50 km in the stratosphere. The EQ observations are described more thoroughly in Nixon et al. (2013).

equatorial data set, one northern pole data set gathered during Titan's mid-northern winter (2005), and another pole data set gathered during late northern winter (2007). These selections were made to begin a preliminary investigation of *n*-butane's possible dependence on latitude and season, expecting to see the established trend of enhanced hydrocarbon abundances in polar data, particularly during winter (Teanby et al. 2019). Each set of observations contains five spectra that were generated by coadding multiple spectra from similar limb altitudes. These altitude ranges and the number of coadded spectra are contained in Table 2. Note that though the FP4 detector of the CIRS instrument does have 10 individual pixels, each of which can record a spectrum, we chose to bin the spectra together by altitude range, yielding five coadded spectra per data set, in consideration of signal-to-noise ratio and computation time during the modeling process. We refer the reader to Nixon et al. (2019) for further details on Cassini CIRS's extensive observations of Titan.

Hereafter, we refer to the data sets in Table 1 by EQ (referring to the equatorial composite data set), T3, or T35, referring to the polar data collected from those respectively named flybys. Each of the three sets of observations we modeled were obtained at the highest resolution available to CIRS (0.5 cm^{-1}). As each of the original data sets were actually sampled, however, at every 0.25 cm^{-1}, we removed every other data point before modeling to ensure correct calculation of goodness-of-fit parameters for our models. Though these FP4 observations covered the spectral range 1025–1495 cm^{-1}, we ultimately focused our search on just the 1300–1495 cm^{-1} region, where *n*-butane's strong ν_{32} and ν_{14} bands are present at 1383 and 1466 cm^{-1}, respectively.

Table 2
Altitude Ranges and Number of Coadded Spectra

Observations	Spectrum ID	Altitudes (km)	No. of Coadded Spectra	Noise (nW cm^{-2} sr^{-1} cm)
T3	1	104–214	38	1.66
	2	162–272	37	2.53
	3	227–337	51	2.35
	4	287–397	48	1.83
	5	352–452	37	1.48
T35	1	113–203	75	0.25
	2	172–262	77	0.60
	3	237–307	68	1.11
	4	293–383	35	1.27
	5	346–456	48	1.21
EQ	1	85–165	356	0.56
	2	110–190	443	0.97
	3	136–216	561	1.23
	4	159–239	570	1.22
	5	177–267	570	0.96

The data were reduced according to the standard CIRS data reduction pipeline as described in Jennings et al. (2017). We extracted individual calibrated CIRS spectra directly from an

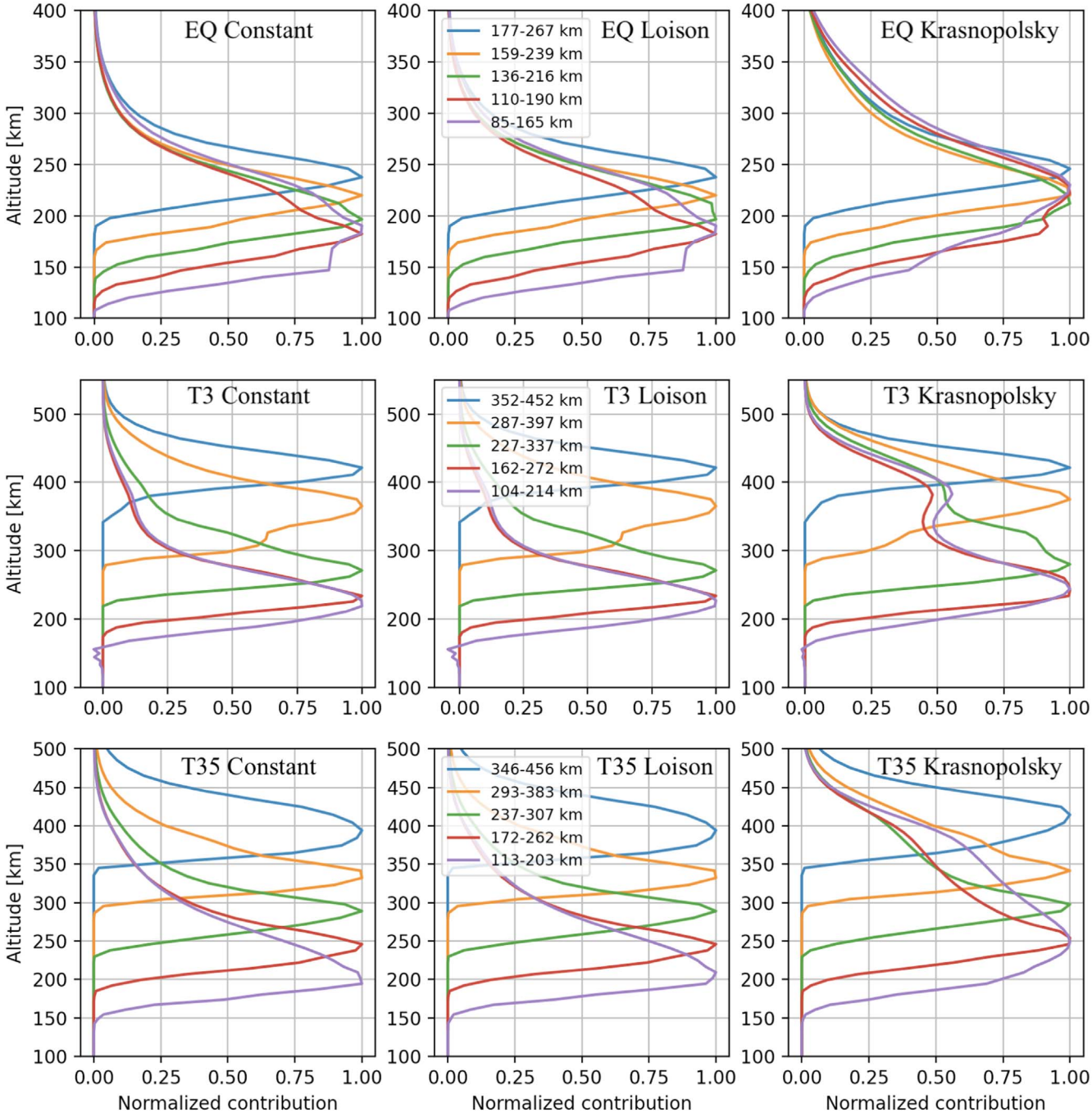

Figure 3. The *n*-butane contribution function curves at 1465 cm^{-1} (near the Q-branch of *n*-butane's ν_{14} band) for each of the nine cases we explored (three data sets, three different profiles). All of our results that follow are reported at the altitudes of the peaks shown in this figure. Note that the legends that appear in the middle panels apply to the other two panels in that row, which belong to the same data set.

internal server at Goddard Space Flight Center with a copy of Planetary Data System Version 4 and performed spectral averaging on these. The noise levels for the observations were estimated by measuring the rms residual between preliminary model fittings and the observations themselves and subsequently fine-tuning the noise level to match the rms in the spectral data.

3. Modeling

We modeled the observations with the Nonlinear Optimal Estimator for MultivariatE Spectral AnalySIS (NEMESIS), which is a planetary atmosphere modeling and retrieval tool (Irwin et al. 2008). NEMESIS has been successfully applied toward the modeling of spectral observations of Titan (and other planetary bodies) in both the infrared and the submillimeter and has been utilized in the detection of multiple new species there (Nixon et al. 2013; Lombardo et al. 2019b; Nixon et al. 2020). We modeled each of the five coadded spectra for a given data set individually in order to extract information specific to that particular altitude bin. A set of a priori altitude profiles for temperature, pressure, and abundances of relevant gases serves as the primary input to a NEMESIS calculation. NEMESIS first generates a forward

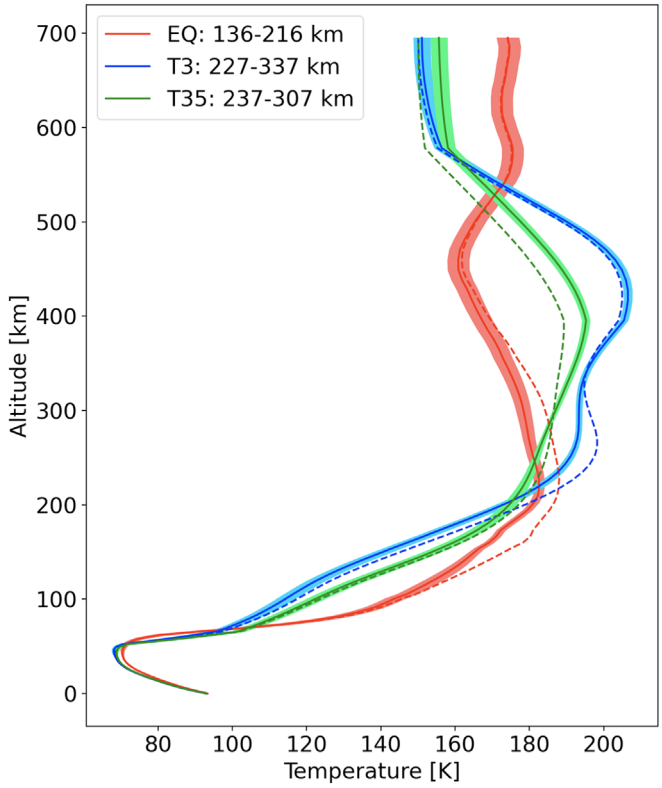

Figure 4. Samples of the retrieved temperature profiles for each of the three data sets (solid curves), as well as the a priori profiles (dashed curves) used in all three cases (Achterberg et al. 2014; Teanby et al. 2019). For each colored curve, the corresponding similarly colored shading identifies the 1σ uncertainty in the retrieved profile.

spectral model from this a priori state. It then compares the forward model to the observations before adjusting the user-selected parameters (such as temperature profile, or gas abundance scaling) to achieve a better fit to the data. In the iterations of this retrieval/inversion model, a fitting algorithm based on the optimal estimation technique described in Rodgers (2000) is utilized. This technique attempts to minimize a cost function similar to a χ^2 goodness-of-fit metric. During an iteration of the fitting, the solution that NEMESIS derives is penalized for deviating from both the a priori state and the model generated in the previous iteration. Specifically, Marquart–Levenberg minimization is used by NEMESIS in order to descend a downhill trajectory with respect to the cost function until satisfactory convergence is attained, meaning that the newly calculated solution changes by less than 0.1% during the final iteration.

Spectral line data from the High-Resolution Transmission Molecular Absorption database (Gordon et al. 2017) were implemented in the modeling of emissions from methane (CH_4), ethane (C_2H_6), ethene (C_2H_4), ethyne (C_2H_2), and hydrogen cyanide (HCN), all of which are spectrally active in the range 1300–1500 cm^{-1}. Pseudoline lists derived at NASA Jet Propulsion Laboratory (JPL), on the other hand, were utilized for modeling of the emissions in this range from propane (C_3H_8; Sung et al. 2013) and propene (C_3H_6; Sung et al. 2018). A newly derived pseudoline list for n-C_4H_{10} (Sung et al. 2020) was implemented in the modeling of potential emissions from n-C_4H_{10}.

Our methodology closely follows that of Lombardo et al. (2019c), who modeled the ν_4, ν_8, and ν_{12} bands of ethane in CIRS FP4 data. First, by fixing the abundance of methane in our model, we retrieved a temperature profile for each of the three sets of observations by modeling methane's ν_4 band at 1305 cm^{-1} using a methane abundance profile that was based on measurements from the Cassini Huygens GCMS instrument (Niemann et al. 2010). This profile assumes a constant methane abundance of 1.48% above 84.6 km, consistent with photochemical models (Wilson 2004).

In Figure 2, we show an example of our model's normalized temperature contribution functions in the region of methane's ν_4 band, showing particular sensitivity to the altitude range 125–350 km. We then show the contributions from n-butane in Figure 3, which displays the altitudes at which each of the spectra we modeled is sensitive to n-butane emission, for each of the three n-butane profiles we tested.

The retrieved temperature profiles for all three data sets, as well as the a priori temperature profiles used, are shown in Figure 4. The a priori temperature profile for the equatorial data comes from the T126 flyby and was derived following the method of Achterberg et al. (2014). The a priori temperature profiles for the two polar data sets (T3 and T35), on the other hand, come from retrievals from Teanby et al. (2019) that were as close as possible to the correct latitude and solar elongation angle for the respective flyby. We then fixed the retrieved temperature profiles in place, subsequently retrieving abundances for ethane, ethene, ethyne, propane, propene, and hydrogen cyanide. Sets of forward models were then generated from these results, in which we systematically introduced varying abundances of n-butane. This was done across the spectral range 1300–1495 cm^{-1}. A sample spectral fit is included in Figure 5, which shows a section (1425–1495 cm^{-1}) of our model for the EQ observations both with and without n-butane, focused on the region containing n-butane's ν_{14} vibrational band at 1466 cm^{-1}, which is its strongest infrared feature. It can be seen there that no strong line-like features are fitted to below the noise level by the n-butane model; instead, aggregate improvement to the fit occurs for the n-butane model. This description is consistent with all of our other results as well. With this consideration in mind, n-butane is not explicitly detected in our work; instead, we were able to derive upper limits on its abundance at various altitudes in each of the three sets of observations, in addition to quantifying the statistical significance in the improvement to the fit when including varying amounts of the target gas. Further details on this are contained in Sections 4 and 5.

From the resulting χ^2 goodness-of-fit metrics for the models with target gas abundance q and the χ^2 of the original model, which was totally free of the target gas ($q = 0$), we calculated the difference $\Delta\chi^2 = \chi_q^2 - \chi_0^2$ and plotted this parameter as a function of target gas abundance q. Note that in this case, $\chi^2 = \sum_\alpha [(D_\alpha - M_\alpha)/\sigma_\alpha]^2$, with D_α being the data spectrum, M_α being the model spectrum, and σ_α being the estimate of the spectral noise, with the index α running over all spectral points in the observation. A good fit occurs for $\chi^2 \approx n - m$, where n is the number of spectral points, and m is the number of degrees of freedom (i.e., number of parameters retrieved) in the model's calculation. The resulting $\Delta\chi^2$ curve marks an improving model fit to the observations as it decreases below zero; conversely, $\Delta\chi^2$ increasing above zero marks a degrading fit to the observations. If the negative minimum of $\Delta\chi^2$ reaches a value β^2, this implies an improvement to the fit of the

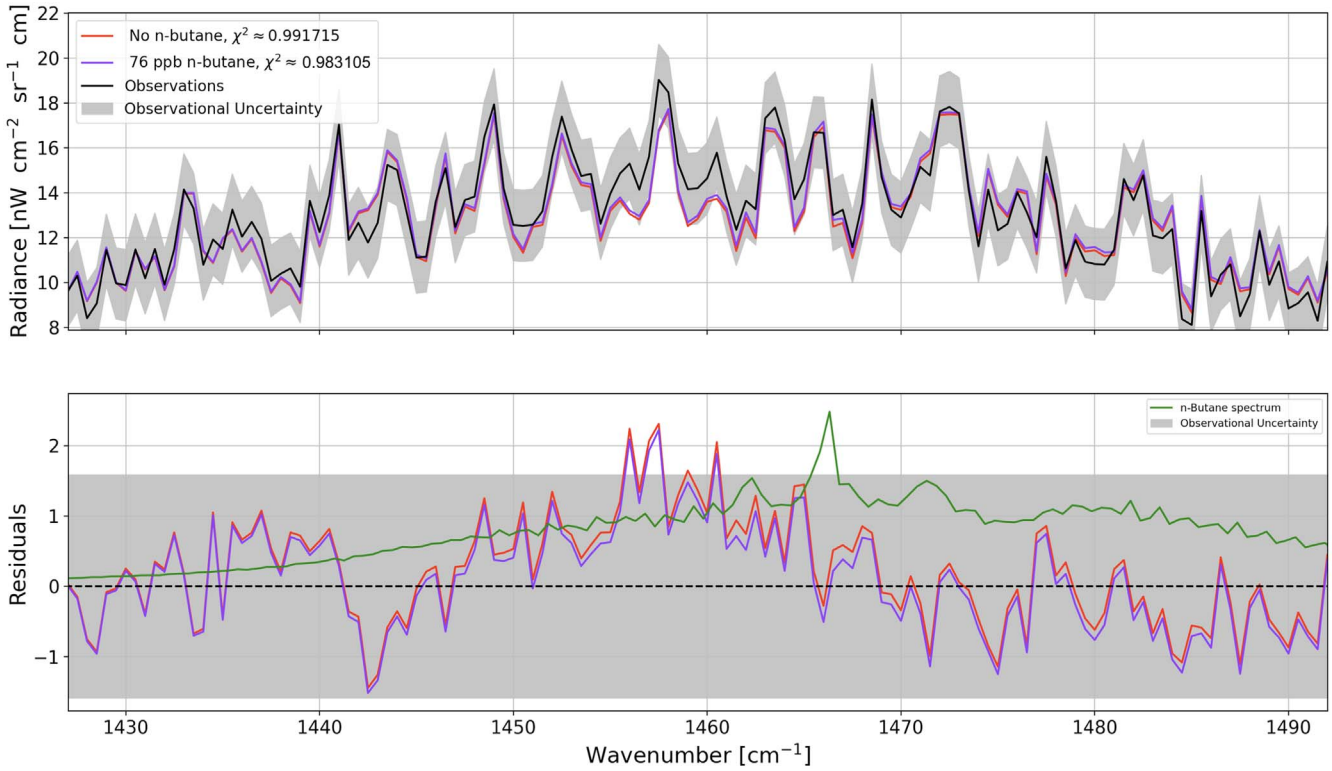

Figure 5. Example of the model fit of the Cassini CIRS observations using the constant altitude profile for *n*-butane. Top: model excluding *n*-butane (red curve) and including 76 ppb of *n*-butane (purple curve), with EQ observations for altitude range 136–216 km (black curve) and 1σ noise envelope in gray. Bottom: residuals (data minus model) following the same color scheme, with an additional green curve overlaid showing *n*-butane's laboratory transmission spectrum at a cold temperature, ~200 K (Sung et al. 2020), convolved to the CIRS resolution (0.5 cm^{-1}). The Q-branch of *n*-butane's ν_{14} band can be seen at 1466 cm^{-1}, though its sharp peak is substantially broadened at CIRS resolution. Improvement to the fit is particularly evident around this ν_{14} region, where the residuals are closer to zero for the purple curve than the red curve.

Table 3
Upper Limits for EQ Data

Profile	ID	Peak Altitude (km)	1σ (ppb)	2σ (ppb)	3σ (ppb)	Minimum (σ)	Abundance (ppb)
Constant (EQ)	1	190	166	214	272	1.23	76
	2	183	162	214	274	1.11	76
	3	197	192	246	299	1.25	76
	4	220	169	230	292	0.98	76
	5	238	143	212	282	0.72	54
Loison (EQ)	1	230	186	239	304	1.21	40
	2	221	174	229	294	1.12	74
	3	212	199	254	320	1.26	74
	4	220	173	234	303	0.98	92
	5	247	146	214	287	0.72	74
Krasnopolsky (EQ)	1	190	99	131	167	1.15	54
	2	182	77	101	130	1.12	46
	3	198	111	142	179	1.27	31
	4	220	111	152	196	0.99	46
	5	238	102	150	203	0.72	47

Note. Shown are 1σ, 2σ, and 3σ upper limits for EQ data, derived from $\Delta\chi^2$ curves using the constant profile and the photochemically predicted profiles of Loison (2019) and Krasnopolsky (2014). These are reported at the peak altitudes of the *n*-butane contribution functions shown in Figure 3. The strengths of the resulting minima in the curves (also measured in σ) are shown as well, in addition to the gas abundance (in ppb) corresponding to that minimum.

observations of statistical significance $\beta\sigma$ relative to the model, which is totally free of the target gas. Similarly, where the $\Delta\chi^2$ curve becomes positive again and reaches a value ϵ^2, this marks an upper bound constraint on the target gas abundance of statistical confidence $\epsilon\sigma$. An example of the retrieved $\Delta\chi^2$ curves is shown and discussed in Section 4, and the full results (upper limits and $\Delta\chi^2$ curve minima) are also compiled in Tables 3–5. The full set of the actual $\Delta\chi^2$ plots is contained in the Appendix. Additionally, all of our spectral fittings are made available to the reader online.

Table 4
Upper Limits for T3 Data

Profile	ID	Altitude (km)	1σ (ppb)	2σ (ppb)	3σ (ppb)	Minimum (σ)	Abundance (ppb)
Constant (T3)	1	223	423	623	864	0.66	163
	2	235	336	527	718	0.55	109
	3	272	177	367	556	⋯	⋯
	4	367	381	703	1046	0.15	54
	5	425	861	1675	2521	0.73	0.01
Loison (T3)	1	247	427	643	874	0.66	149
	2	245	339	530	733	0.55	112
	3	278	178	370	563	⋯	⋯
	4	375	384	716	1030	0.15	55
	5	422	678	1540	2449	⋯	⋯
Krasnopolsky (T3)	1	225	190	289	392	0.61	63
	2	230	149	232	323	0.54	51
	3	274	107	222	337	⋯	⋯
	4	363	397	739	1069	0.15	50
	5	423	706	1619	2550	⋯	⋯

Note. Shown are 1σ, 2σ, and 3σ upper limits for T3 data. Note that the ellipses marking empty entries in the table correspond to instances where a minimum in the $\Delta\chi^2$ curve was not observed.

Table 5
Upper Limits for T35 Data

Profile	ID	Altitude (km)	1σ (ppb)	2σ (ppb)	3σ (ppb)	Minimum (σ)	Abundance (ppb)
Constant (T35)	1	195	212	330	456	0.57	76
	2	248	87	187	289	⋯	⋯
	3	290	85	224	369	⋯	⋯
	4	335	325	585	859	0.19	55
	5	395	552	1102	1653	⋯	⋯
Loison (T35)	1	248	216	337	466	0.57	62
	2	253	88	190	292	⋯	⋯
	3	298	85	225	373	⋯	⋯
	4	345	325	595	862	0.19	56
	5	421	551	1080	1619	⋯	⋯
Krasnopolsky (T35)	1	207	78	123	169	0.53	75
	2	247	53	113	173	⋯	⋯
	3	290	64	168	280	⋯	⋯
	4	335	266	485	709	0.18	56
	5	392	577	1140	1709	⋯	⋯

We employed the $\Delta\chi^2$ procedure for three different test profiles for *n*-butane: (1) a step function profile that activates at 70 km above the surface of Titan and remains at a constant abundance above this point, (2) the photochemically predicted profile for butane from Krasnopolsky (2009), and (3) the photochemically predicted profile for butane from Loison (2019). These profiles are displayed in Figure 6.

4. Results

Our results are represented here by a sample of the retrieved $\Delta\chi^2$ curves. This sample, shown in Figure 7, was obtained from the EQ observations and used the constant *n*-butane profile. This particular outcome shows that while adding *n*-butane to the model (particularly with an abundance of approximately 80 ppb) does improve the fit to the observations, the statistical significance of this improvement is not substantial. The $\Delta\chi^2$ curves for the other profiles that we tested and the other data sets and their corresponding altitude ranges are contained in the Appendix to promote readability of the main body of this paper. For convenience, however, we compile all of the information contained in each of our retrieved $\Delta\chi^2$ curves in Tables 3–5 in this section.

We also display in this section plots of the three profiles we tested overlaid with the retrieved 1σ, 2σ, and 3σ abundance upper limits. These are shown in Figures 8, 9, and 10 for the EQ, T3, and T35 data sets, respectively. In these figures, the upper limits are reported at the midpoint of the altitude range corresponding to that particular spectrum. Note that the altitude ranges of the individual spectra are recorded in Tables 3–5.

5. Discussion

The *n*-butane molecule, though predicted to be present in Titan's atmosphere by a multitude of photochemical models (e.g., Yung et al. 1984; Lara et al. 1996; Krasnopolsky 2009;

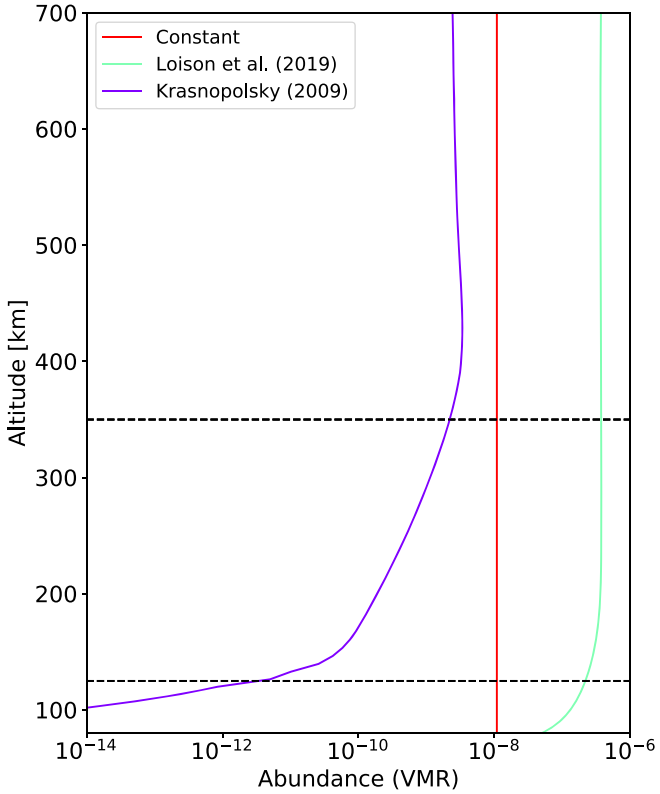

Figure 6. Full gas abundance profiles explored in our work. Black horizontal dashed lines show the approximate altitude region for which our models are sensitive. See Figures 2 and 3 for further details on the sensitivity of our models. Note that the placement of the constant profile (red curve) is arbitrary, since our analysis ultimately included scaling this profile to a set of differing abundances.

Dobrijevic et al. 2016; Loison 2019; Vuitton et al. 2019), has thus far eluded all detection efforts, including this one. In some cases, however, our results do provide tentative evidence for the presence of *n*-butane in Titan's atmosphere.

Recently, Hewett et al. (2020) used infrared cross sections to derive an upper limit of 513 ppb for *n*-butane's abundance. They used the cross sections from the Pacific Northwest National Laboratory (Sharpe et al. 2004), which were obtained at 278 K. As that temperature is closest to (although still significantly warmer than) our retrieved stratospheric temperatures for the EQ data, it is useful to compare those results as a starting point. From Figure 8 and Table 3, it is seen that each of our 3σ upper limits is consistent with the result of Hewett et al. (2020). For instance, using the Loison profile, we find abundances less than 200 ppb in the stratosphere. When using the constant *n*-butane profile rather than the Loison profile (Figure 6), similar improvement in the same altitude ranges is observed. The Krasnopolsky profile also yields similar improvement to the fit.

Importantly, with respect to that prior result, one advantage in our approach is the use of a recently derived high-resolution pseudoline list for *n*-butane from NASA JPL (Sung et al. 2020). That line list constitutes the most detailed and up-to-date spectroscopic representation of *n*-butane at cold temperatures (down to 180 K) and N_2-broadened pressures applicable to remote sensing in Titan's atmosphere. We also used a recent pseudoline list for propene in our models (Sung et al. 2018).

We note here that *n*-butane is likely to condense in Titan's atmosphere slightly below the "activation altitude" of the constant profile that we employed; according to one study by Barth (2017), for example, which modeled the microphysics of cloud formation in Titan's atmosphere, *n*-butane is likely to condense at altitudes of approximately 65 km above Titan's surface. Thus, the constant profile that we employed is rendered valid by that study.

Lastly, examining the upper limits plotted in Figure 8, we see that the photochemically predicted *n*-butane profile of Loison (2019) appears to be potentially ruled out in the case of equatorial latitudes across the full altitude range of sensitivity; each 3σ upper limit occurs at an abundance about 15% lower than the predicted abundance in the profile. Of course, as we have not yet confirmed the presence of *n*-butane in Titan's atmosphere, it is difficult to say with confidence that this analysis invalidates the Loison (2019) prediction in this case.

With that noted, we bring this discussion to a close by pointing out a possible weakness in our analysis, all of which is largely statistical in nature. The definition of $\Delta\chi^2$ as discussed in Section 3 relies strongly on our estimate of the noise level in the spectra. We have assumed that the noise has Gaussian (i.e., white-noise) properties that can be well estimated by the rms across the spectral residuals. In some cases, particularly the EQ data, the residuals show that this assumption is not valid, and that a vibrational band of at least one gas, either ethane or propane, is not perfectly fitted by our model. We tested our results' dependence on this by also retrieving ethane and propane altitude profiles, rather than just scalings of the a priori profiles. While some improvement to the fit (reduced and more Gaussian-like residuals) was observed, the improvement was not significant and mattered little in the context of our subsequent $\Delta\chi^2$ analysis with *n*-butane. Because of this, a substantial portion of the non-Gaussian, continuum-like features occasionally observed in our residuals is thought to arise from imperfect fitting of hazes in that spectral region.

With all of this in mind, we encourage the reader to consider these results as a step in the right direction toward understanding *n*-butane's possible role in Titan's atmosphere and chemistry, rather than as incontrovertible evidence in favor of its presence or of one or the other abundance profiles that we tested. Further work, perhaps involving higher-resolution observations, will likely contribute to solidifying or disqualifying the results presented here. Nevertheless, our results are still expected to be helpful in constraining any photochemical models that include *n*-butane.

6. Conclusions

We have obtained new upper-limit constraints on the abundance of *n*-C_4H_{10} in Titan's stratosphere. These were obtained for a variety of atmospheric profiles either photochemically predicted or set as constant above 70 km (Krasnopolsky 2009; Loison 2019). In all cases, our results are consistent with previous upper limits for *n*-butane established in the literature (Hewett et al. 2020). Though *n*-butane has certainly not been firmly detected through our work, we have demonstrated tentative statistical evidence for its presence within Titan's stratosphere, particularly in observations of Titan's equator. These results can be utilized to extend the search for *n*-butane via future higher-resolution observations, either from ground-based observatories, such

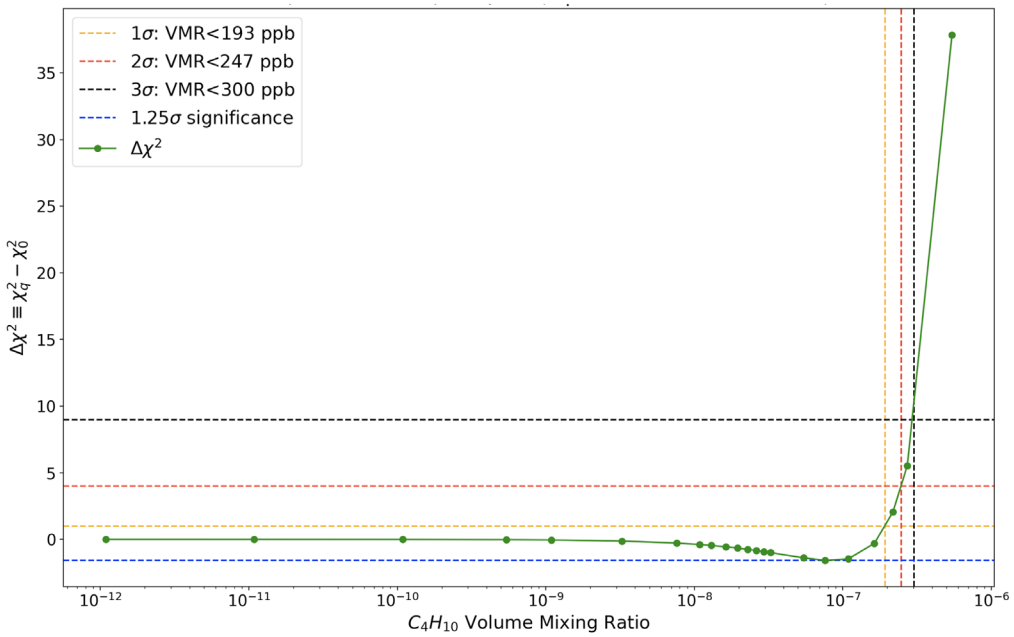

Figure 7. Sample $\Delta\chi^2$ curve for the 136–216 km EQ data using the constant *n*-butane profile. Improvement to the fit is seen for *n*-butane abundances of about 80 ppb, though the statistical significance of that improvement is fairly small (1.25σ). The 1σ, 2σ, and 3σ upper limits on the *n*-butane abundance are marked by dashed vertical lines, as labeled in the legend.

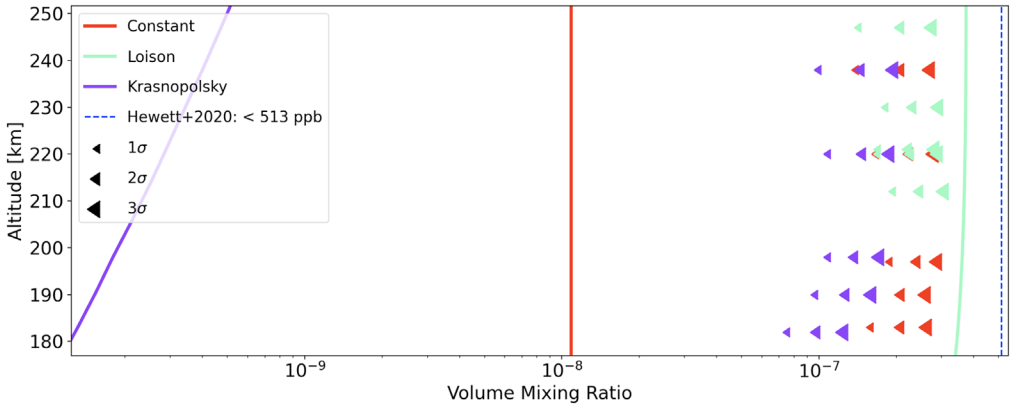

Figure 8. The 1σ, 2σ, and 3σ upper limits for *n*-butane's abundance, marked by left-pointing arrows, using the EQ data set. The colors of the upper-limit points correspond to the similarly colored profile curves. The vertical blue dashed line marks the upper limit (513 ppb) derived by Hewett et al. (2020), discussed further in Section 5.

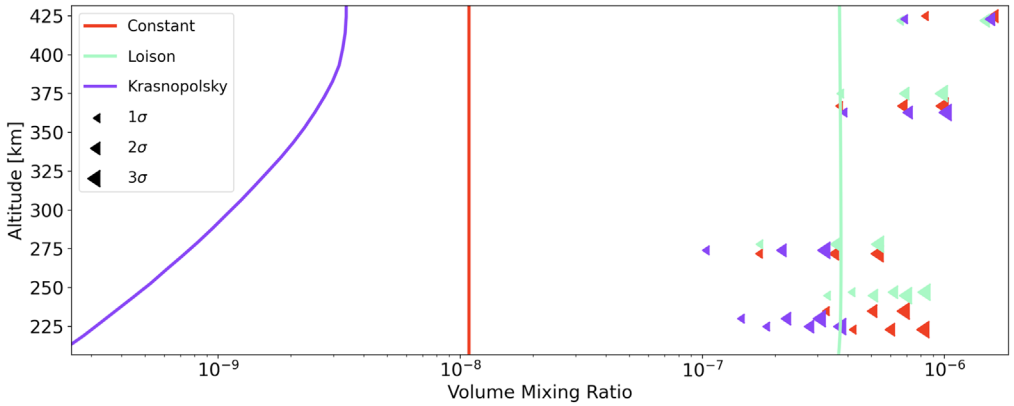

Figure 9. The 1σ, 2σ, and 3σ upper limits for *n*-butane's abundance, marked by left-pointing arrows, using the T3 data set. The colors of the upper-limit points correspond to the similarly colored profile curves.

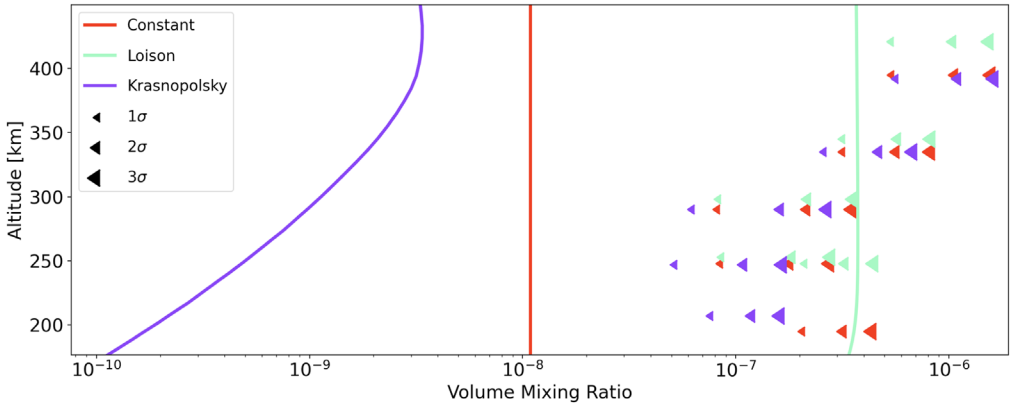

Figure 10. The 1σ, 2σ, and 3σ upper limits for *n*-butane's abundance, marked by left -pointing arrows, using the T35 data set. The colors of the upper-limit points correspond to the similarly colored profile curves.

as NASA's IRTF, or from upcoming orbital platforms (e.g., the James Webb Space Telescope).

We would like to acknowledge the Planetary Data System, which we used to obtain our observations. Part of the research was performed at the Jet Propulsion Laboratory, California Institute of Technology, under contracts with the National Aeronautics and Space Administration. P.G.J.I. acknowledges the support of the UK Science and Technology Facilities Council. C.A.N. was supported by the NASA Astrobiology Institute for his contributions to this work. B.L.S. wishes to thank Goddard Space Flight Center for their continuous support of this work.

Appendix

The remainder of the $\Delta\chi^2$ curves not shown in the main body of this paper are collected here, in Figures 11–19. For readability of the Appendix, we also include the $\Delta\chi^2$ curve obtained for the EQ data using the constant profile, even though this was the example shown in the main text. We note once again that all of our spectral fittings for each of the cases shown below are also available to the reader online. In each figure, each of the panels is labeled by its spectrum ID (Table 1) and *n*-butane contribution function peak altitude.

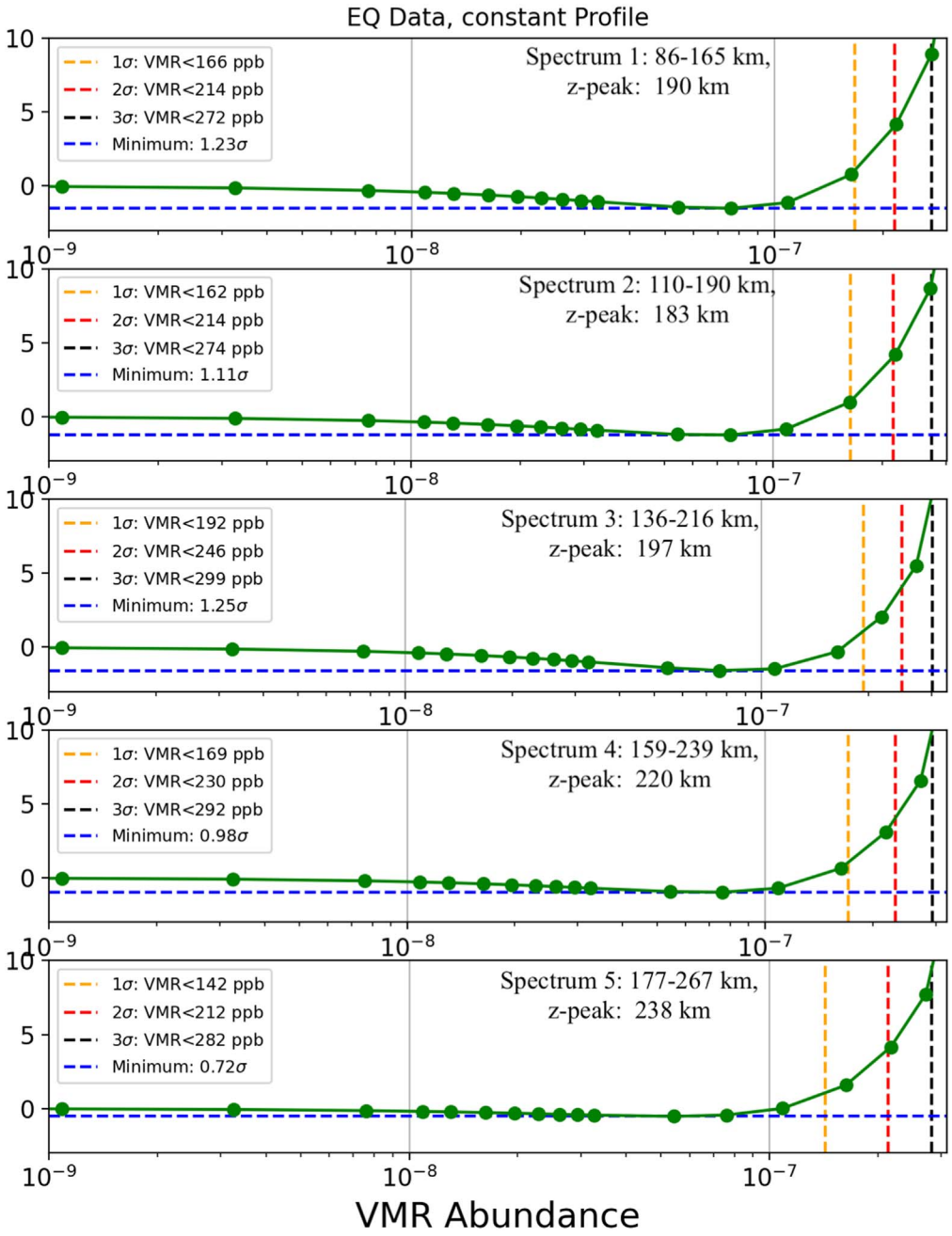

Figure 11. The $\Delta\chi^2$ curve for EQ data using the constant *n*-butane profile.

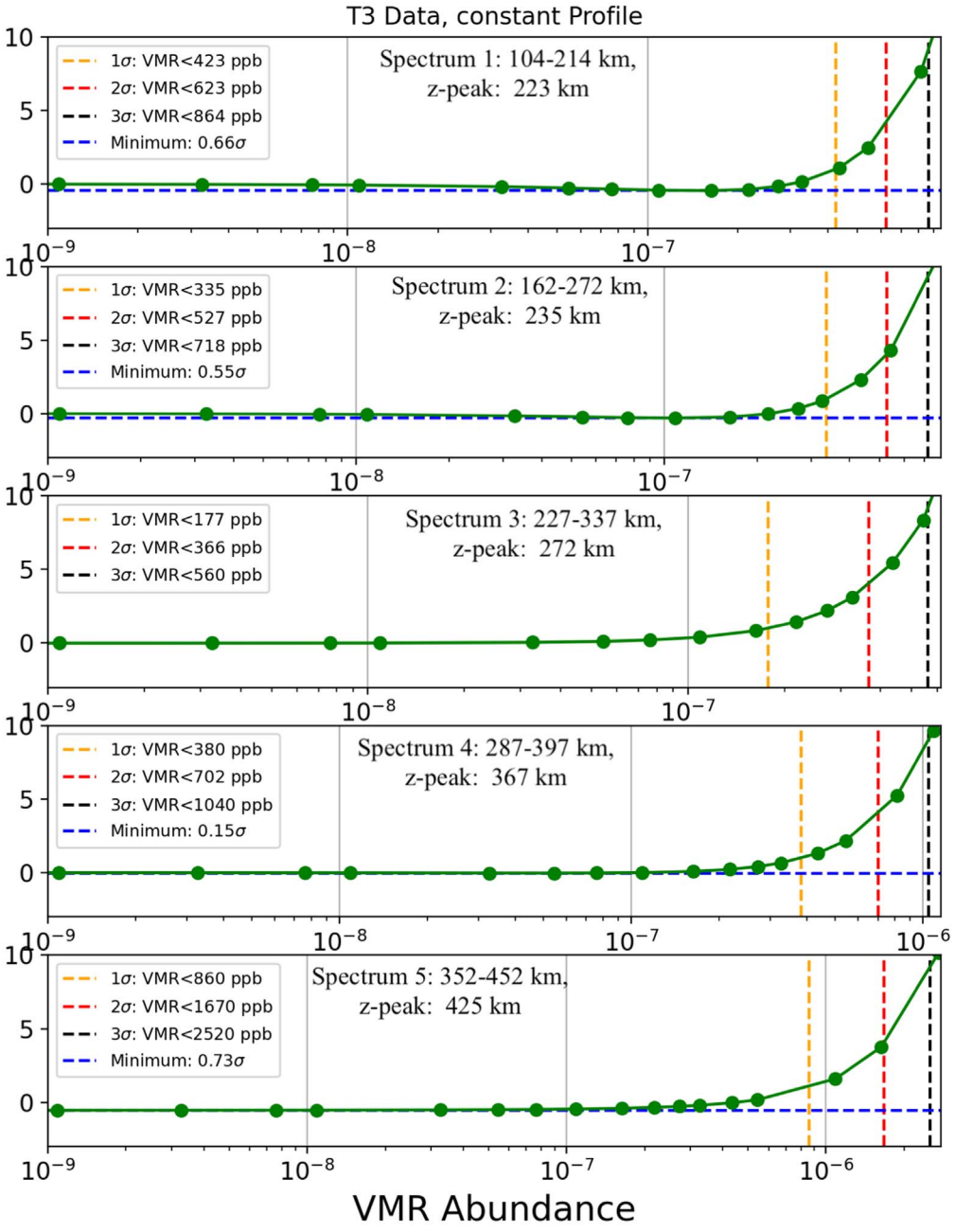

Figure 12. The $\Delta\chi^2$ curve for T3 data using the constant *n*-butane profile.

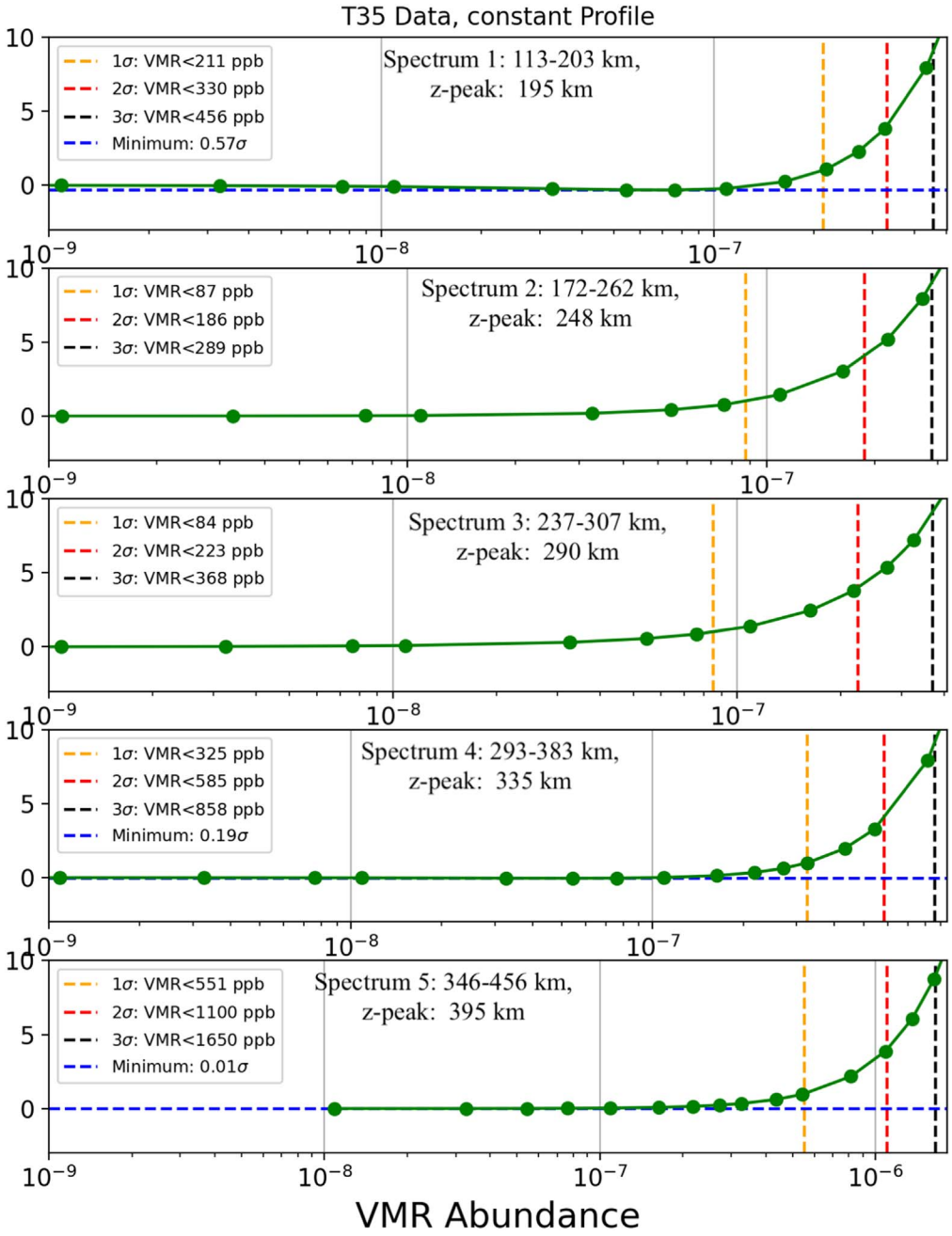

Figure 13. The $\Delta\chi^2$ curve for T35 data using the constant *n*-butane profile.

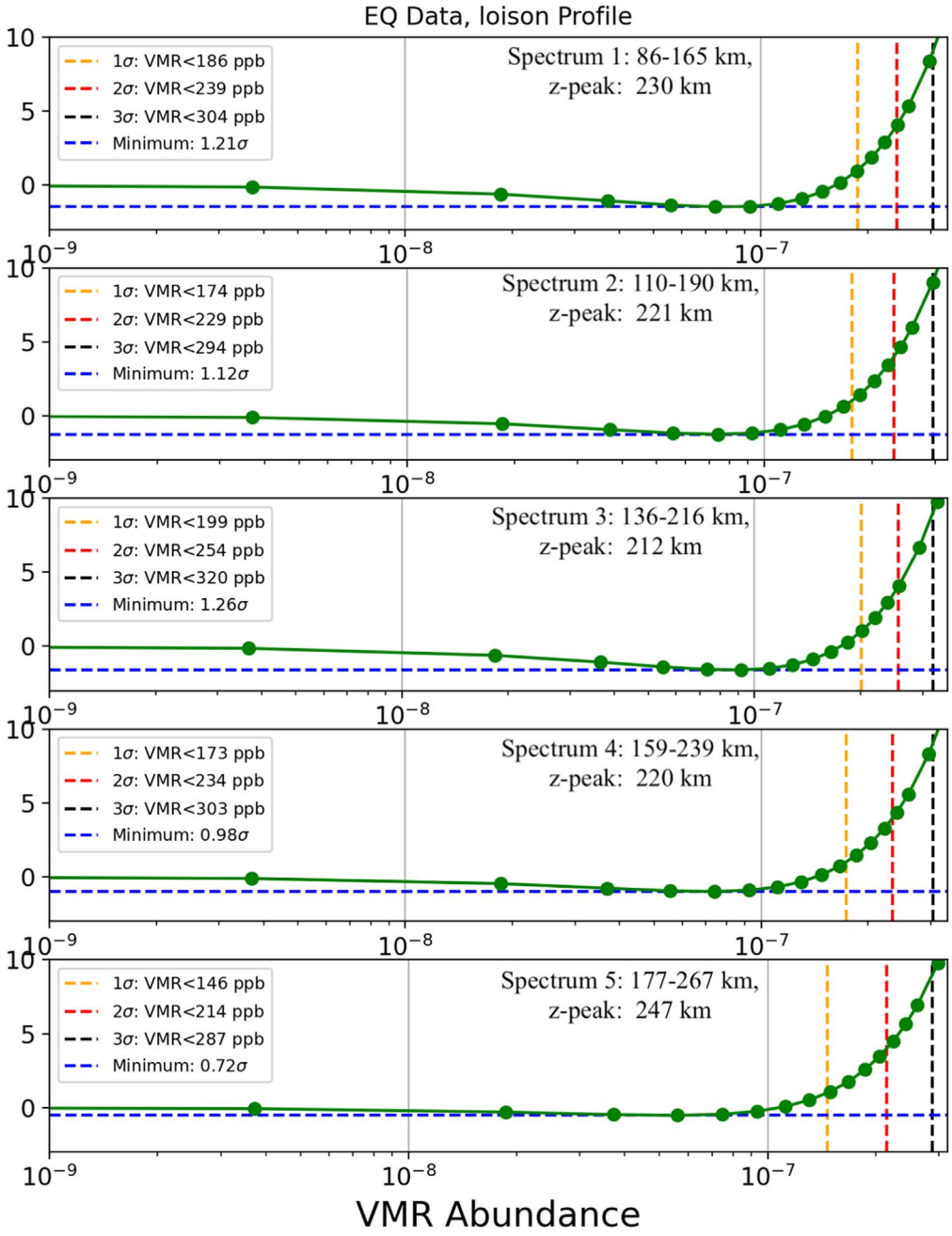

Figure 14. The $\Delta\chi^2$ curve for EQ data using the Loison *n*-butane profile.

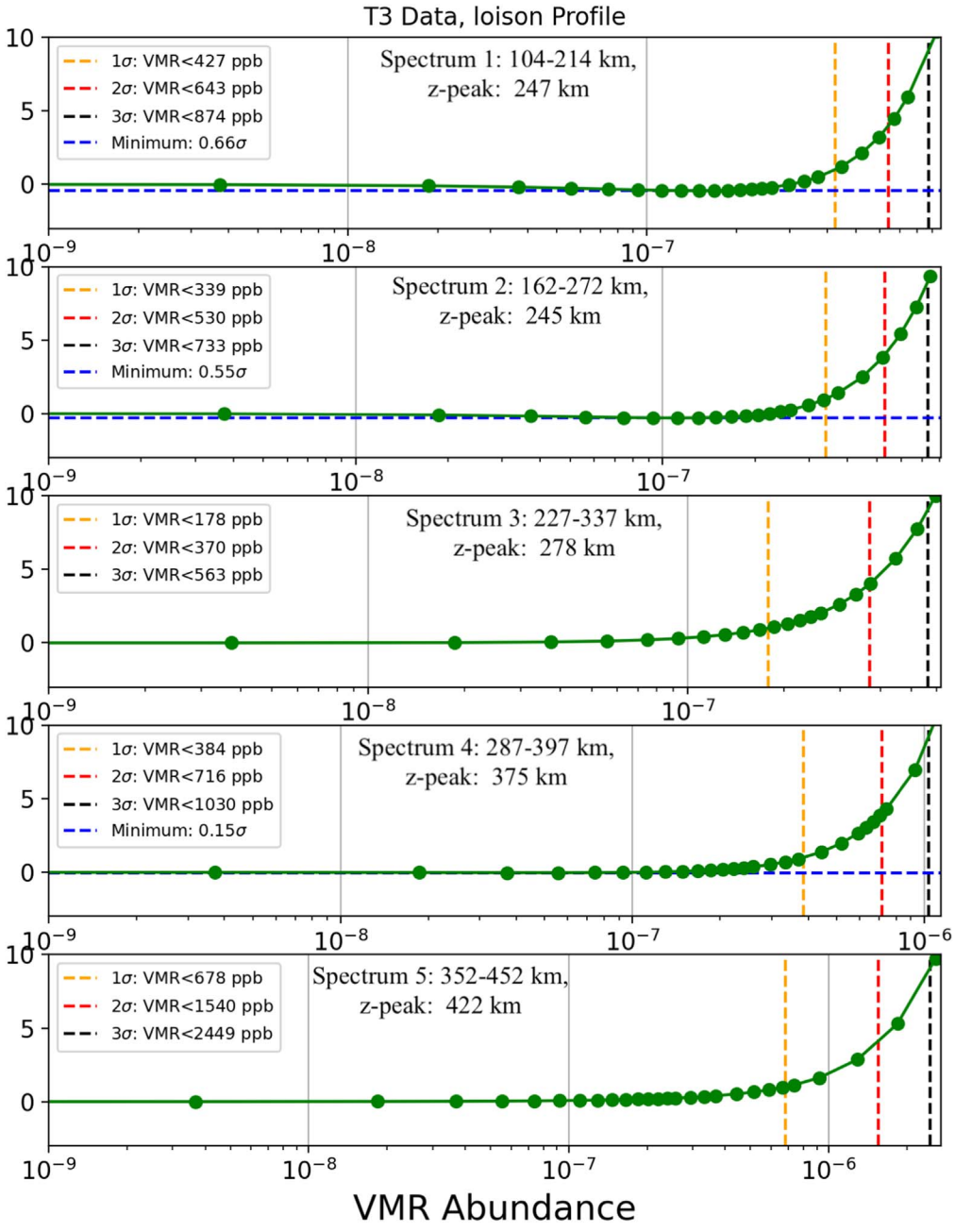

Figure 15. The $\Delta\chi^2$ curve for T3 data using the Loison *n*-butane profile.

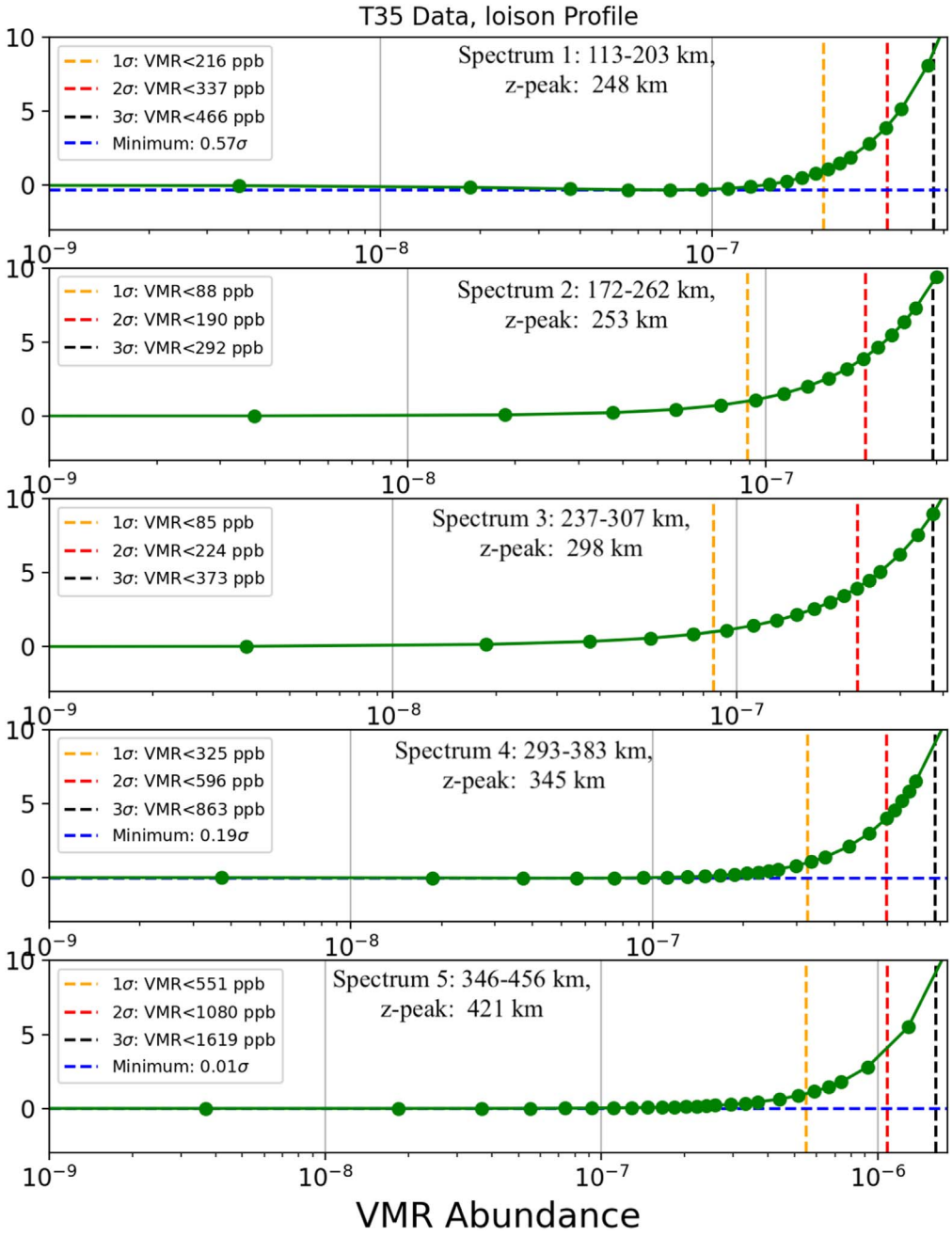

Figure 16. The $\Delta\chi^2$ curve for T3 data using the Loison *n*-butane profile.

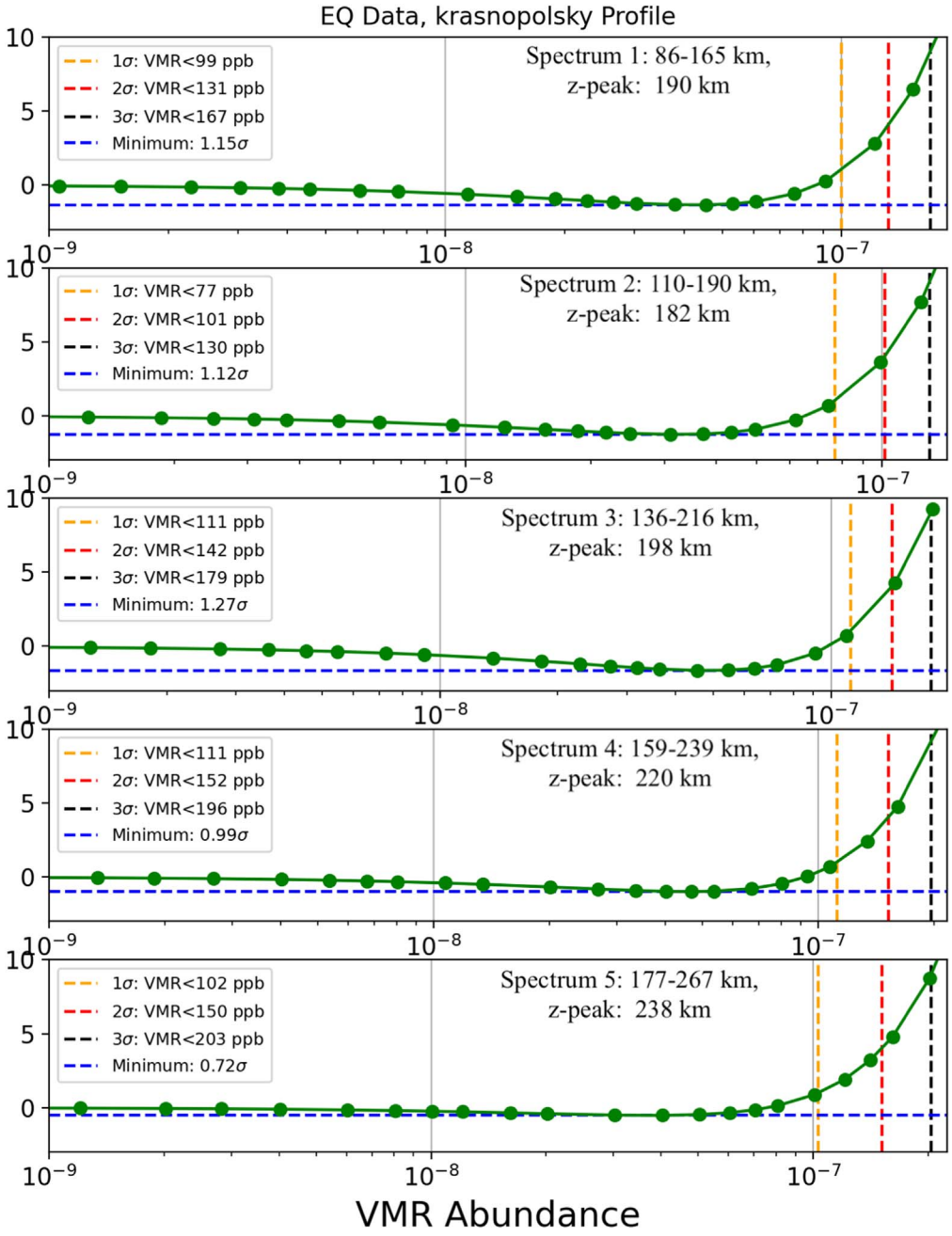

Figure 17. The $\Delta\chi^2$ curve for EQ data using the Krasnopolsky *n*-butane profile.

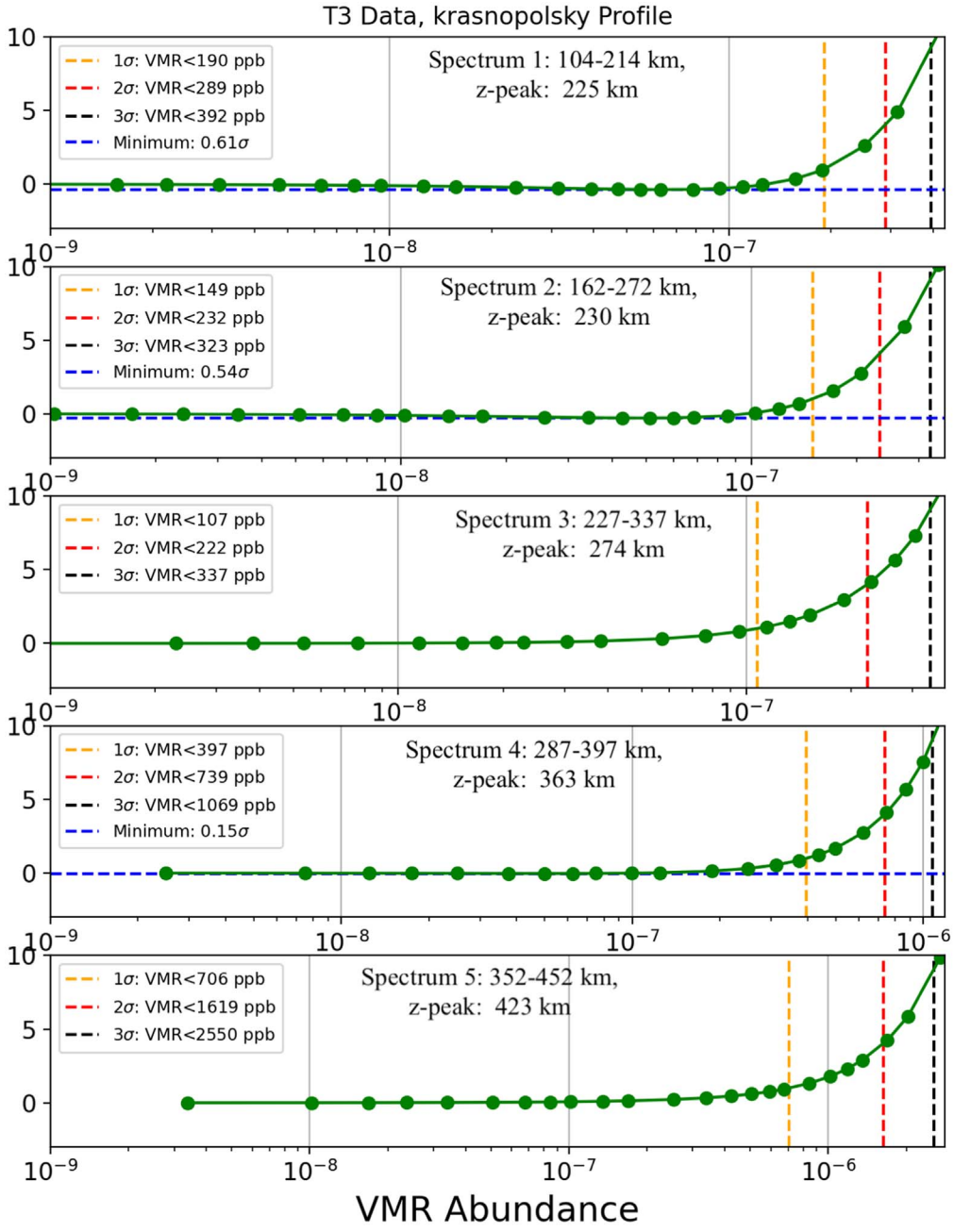

Figure 18. The $\Delta\chi^2$ curve for T3 data using the Krasnopolsky *n*-butane profile.

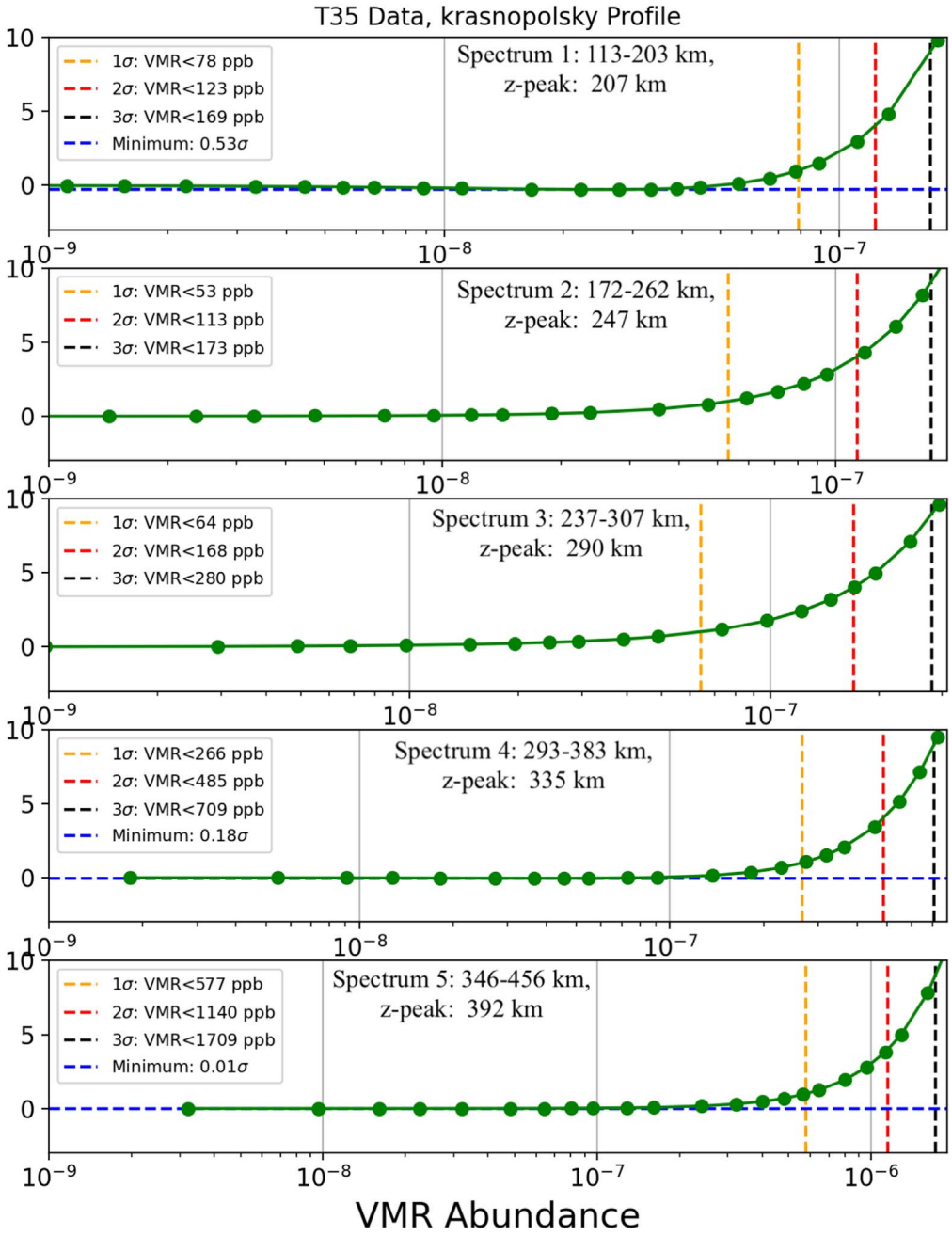

Figure 19. The $\Delta\chi^2$ curve for T35 data using the Krasnopolsky *n*-butane profile.

ORCID iDs

Brendan L. Steffens https://orcid.org/0000-0001-6587-4145
Conor A. Nixon https://orcid.org/0000-0001-9540-9121
Keeyoon Sung https://orcid.org/0000-0002-8030-7410
Patrick G. J. Irwin https://orcid.org/0000-0002-6772-384X
Nicholas A. Lombardo https://orcid.org/0000-0001-8621-6520

References

Achterberg, R. K., Gierasch, P. J., Conrath, B. J., et al. 2014, AAS/DPS Meeting, 46, 102.07
Ádámkovics, M., & Boering, K 2003, JGRE, 108, 5092
Barth, E. L. 2017, P&SS, 137, 20
Bézard, B., Marten, A., & Paubert, G. 1993, AAS/DPS Meeting, 25, 25.09
Cordiner, M. A., Palmer, M. Y., Nixon, C. A., et al. 2015, ApJL, 800, L14
Cottini, V., Nixon, C. A., Jennings, D. E., et al. 2012, Icar, 220, 855
Coustenis, A., Jennings, D. E., Achterberg, R. K., et al. 2016, Icar, 270, 409
Coustenis, A., Jennings, D. E., Achterberg, R. K., et al. 2018, ApJL, 854, L30
Coustenis, A., Salama, A., Schulz, B., et al. 2003, Icar, 161, 383
Coustenis, A., & Taylor, F. 2008, Titan: Exploring an Earthlike World, 2nd ed. (Singapore: World Scientific)
Curtis, D. B., Glandorf, D. L., Toon, O. B., et al. 2005, JPCA, 109, 1382
Dobrijevic, M., Loison, J., Hickson, K., & Gronoff, G. 2016, Icar, 268, 313
Flasar, F. M., Kunde, V. G., Abbas, M. M., et al. 2004, SSRv, 115, 169
Gordon, I., Rothman, L., Hill, C., et al. 2017, JQSRT, 203, 3
Hewett, D., Bernath, P. F., Wong, A., et al. 2020, Icar, 344, 113460
Irwin, P., Teanby, N., de Kok, R., et al. 2008, JQSRT, 109, 1136
Jennings, D. E., Flasar, F. M., Kunde, V. G., et al. 2017, ApOpt, 56, 5274
Kim, Y. S., Bennett, C. J., Chen, L.-H., O'Brien, K., & Kaiser, R. I. 2010, ApJ, 711, 744
Krasnopolsky, V. A. 2009, Icar, 201, 226
Krasnopolsky, V. A. 2014, Icar, 236, 83
Lara, L. M., Lellouch, E., López-Moreno, J. J., & Rodrigo, R. 1996, JGR, 101, 23261
Li, C., Zhang, X., Gao, P., & Yung, Y. 2015, ApJL, 803, L19
Loison, J. C., Dobrijevic, M., & Hickson, K.M. 2019, Icar, 329, 55
Lombardo, N. A., Nixon, C. A., Achterberg, R. K., et al. 2019a, Icar, 317, 454
Lombardo, N. A., Nixon, C. A., Greathouse, T. K., et al. 2019b, ApJL, 881, L33
Lombardo, N. A., Nixon, C. A., Sylvestre, M., et al. 2019c, AJ, 157, 160
Lopes, R. M., Peckyno, R. S., Le Gall, A. A., et al. 2010, AGUFM, 2010, P31C-1548
Maguire, W., Hanel, R.A., Jennings, D.E., Kunde, V. G., & Samuelson, R. E. 1981, Natur, 292, 683
Mathé, C., Vinatier, S., Bézard, B., et al. 2020, Icar, 344, 113547
Niemann, H. B., Atreya, S. K., Demick, J. E., et al. 2010, JGR, 115, E12006
Nixon, C., Jennings, D., Flaud, J.-M., et al. 2009, P&SS, 57, 1573
Nixon, C. A., Ansty, T. M., Lombardo, N. A., et al. 2019, ApJS, 244, 14
Nixon, C. A., Jennings, D. E., Bézard, B., et al. 2013, ApJL, 776, L14
Nixon, C. A., Thelen, A. E., Cordiner, M. A., et al. 2020, AJ, 160, 205
Palmer, M. Y., Cordiner, M. A., Nixon, C. A., et al. 2017, SciA, 3, e1700022
Rodgers, C. D. 2000, Inverse Methods for Atmospheric Sounding (Singapore: World Scientific)
Roe, H.G., Greathouse, T.K., & Richter, M.J. 2003, ApJL, 597, L65
Sharkey, J., Teanby, N.A., & Sylvestre, M. 2021, Icar, 354, 114030
Sharpe, S. W., Johnson, T. J., Sams, R. L., et al. 2004, ApSpe, 58, 1452
Sung, K., Steffens, B., Toon, G., Nemchick, D., & Smith, M. A. 2020, JQSRT, 251, 107011
Sung, K., Toon, G. C., Drouin, B. J., Mantz, A. W., & Smith, M. A. H. 2018, JQSRT, 213, 119
Sung, K., Toon, G. C., Mantz, A. W., & Smith, M. A. H. 2013, Icar, 226, 1499
Teanby, N., Irwin, P., de Kok, R., et al. 2009, Icar, 202, 620
Teanby, N. A., Sylvestre, M., Sharkey, J., et al. 2019, GeoRL, 46, 3079
Thelen, A. E., Cordiner, M. A., Nixon, C. A., et al. 2020, ApJL, 903, L22
Trainer, M. 2013, Current Organic Chemistry, 17, 1710
Vinatier, S., Bézard, B., Lebonnois, S., et al. 2015, Icar, 250, 95
Vinatier, S., Mathé, C., Bézard, B., et al. 2020, A&A, 641, A116
Vuitton, V., Yelle, R., Klippenstein, S., Hörst, S., & Lavvas, P. 2019, Icar, 324, 120
Willacy, K., Allen, M., & Yung, Y. 2016, ApJ, 829, 79
Wilson, E. H. 2004, JGR, 109, E06002
Yung, Y. L., Allen, M., & Pinto, J. P. 1984, ApJS, 55, 465